PHYSICAL REVIEW C **72**, 034606 (2005)

Elastic scattering of the proton drip-line nucleus ^{17}F

J. C. Blackmon,[1] F. Carstoiu,[2,3] L. Trache,[2] D. W. Bardayan,[1] C. R. Brune,[4] C. A. Gagliardi,[2] U. Greife,[5] C. J. Gross,[1] C. C. Jewett,[5] R. L. Kozub,[6] T. A. Lewis,[1] J. F. Liang,[1] B. H. Moazen,[6] A. M. Mukhamedzhanov,[2] C. D. Nesaraja,[1,6] F. M. Nunes,[7] P. D. Parker,[8] L. Sahin,[9] J. P. Scott,[1,6] D. Shapira,[1] M. S. Smith,[1] J. S. Thomas,[10] and R. E. Tribble[2]

[1]*Physics Division, Oak Ridge National Laboratory, Oak Ridge, TN 37831, USA*
[2]*Cyclotron Institute, Texas A&M University, College Station, Texas 77843-3366, USA*
[3]*National Institute for Physics and Nuclear Engineering "Horia Hulubei," P.O. Box MG-6, RD-76900, Bucharest-Magurele, Romania*
[4]*Department of Physics and Astronomy, Ohio University, Athens, Ohio 45701, USA*
[5]*Department of Physics, Colorado School of Mines, Golden, Colorado 80401, USA*
[6]*Physics Department, Tennessee Technological University, Cookeville, Tennessee 38505, USA*
[7]*National Superconducting Cyclotron Laboratory, Michigan State University, East Lansing, Michigan 48824, USA*
[8]*A. W. Wright Nuclear Structure Laboratory, Yale University, New Haven, Connecticut 06511, USA*
[9]*Department of Physics, Dumlupinar University, Kutahya, Turkey 43100*
[10]*Department of Physics and Astronomy, Rutgers University, New Brunswick, New Jersey 08903, USA*

(Received 19 May 2005; published 26 September 2005)

Precision data have been obtained for the elastic scattering of ^{17}F on ^{12}C and ^{14}N at 10 MeV/nucleon to clarify the reaction mechanism for loosely bound nuclei at low energies and to assess the validity of a double-folding procedure to predict optical model potentials for use in indirect methods for nuclear astrophysics. The double-folding procedure incorporates density and energy-dependent effective nucleon-nucleon interactions with realistic densities consistent with experimentally determined asymptotic normalization coefficients. The derived potentials provide an excellent description of the data and point to a complete dominance of absorption at the barrier. A semiclassical analysis in terms of multireflection barrier–internal barrier series expansion of the scattering amplitude shows that only the barrier component survives in the scattering process, pointing to the peripheral character of the reactions.

DOI: 10.1103/PhysRevC.72.034606 PACS number(s): 25.60.Bx, 24.10.−i, 25.60.Dz, 25.60.Gc

I. INTRODUCTION

Heavy-ion elastic-scattering reactions have been a major source of information on the structure of nuclei and the properties of nucleus-nucleus interactions. Global models of nuclear properties have been built based in large part on elastic scattering with stable nuclei and have been used as a basis for extracting structure information from nuclear reaction studies, by use of distorted-wave Born approximation (DWBA) techniques for example. Reaction studies with radioactive nuclear beams (RNBs) are now expanding our understanding of nuclear structure to loosely bound nuclei away from stability. For example, several recent proton-transfer experiments were performed with RNBs at energies around 10 MeV/nucleon, at which reactions are peripheral, with the intention of extracting stellar reaction rates [1–3].

However, nuclear potentials for light nuclei near the drip lines are typically ambiguous and poorly constrained by limited elastic-scattering data, which raises questions about the accuracy and reliability of nuclear structure information extracted from reaction studies in such cases. These nuclei may also exhibit exotic phenomena. Their single-particle structure is dominated by only a few components, typically of low angular momenta. Long tails (or halos) may appear in the single-particle densities, and the total reaction and one-particle-removal cross sections are large. The enhanced density in the tail leads to a competition between the enhanced refractive power of the real potential and the increased absorption that is due to the long-range part of the effective nucleon-nucleon interaction that results sometimes in exotic elastic-scattering angular distributions [4]. The coupling of the elastic channel with breakup and nucleon-transfer channels leads to a dynamic polarization potential (DPP) that is complex and nonlocal, with a complicated mass, energy, and radial dependence.

Understanding reaction mechanisms and the properties of nuclear interactions for loosely bound nuclei is of crucial importance for improving the quality of nuclear structure information extracted from nuclear reaction studies. Previous studies of scattering of *p*-shell nuclei showed that a double-folding procedure with a modified version of the nuclear matter approach of Jeukenne, Lejeune, and Mahaux (JLM) [5] provided a good description of potentials for loosely bound nuclei by use of the normal absorptive component of the JLM nucleon-nucleon interaction. However, the real part of the potential required significant renormalization to account for effects of the DPP [4,6]. In this work we test this description of optical-model potentials for the more loosely bound *sd*-shell nucleus ^{17}F. We measured elastic-scattering angular distributions for the ^{14}N(^{17}F,^{17}F)^{14}N and ^{12}C(^{17}F,^{17}F)^{12}C reactions at 10 MeV/nucleon. This energy is about half of the saturation energy for light nuclei (the energy at which almost all reaction channels are open), and there are indications that traces of an increased transparency in the optical potential could be revealed [4].

The nucleus ^{17}F ($J^\pi = 5/2^+$, $S_{-1p} = 0.600$ MeV) has been involved in many experiments in recent years owing in large part to its development as a RNB at the Argonne National Laboratory (ANL) [7] and the Oak Ridge National

Laboratory (ORNL) [8] and to its role in the hot CNO cycle of reactions that power novae [9]. These measurements have prompted interest in the determination of reliable optical-model potentials for ^{17}F. The proton radiative capture reaction ^{16}O$(p,\gamma)^{17}$F has been measured at stellar energies by Morlock *et al.* [10]. The extracted astrophysical S factors are in excellent agreement with those obtained with the asymptotic normalization coefficient (ANC) method by use of the transfer reaction ^{16}O$(^3$He,$d)^{17}$F by Gagliardi *et al.* [11], and the halo properties of the first excited state ($J^\pi = 1/2^+$, $E_x = 495$ keV) were well established. Quasi-elastic scattering on a heavy target has been measured by Liang *et al.* [12,13] and by Romoli *et al.* [14] at near-barrier energies. Not much information about the nuclear part has been extracted from these studies because the interaction is strongly dominated by Coulomb repulsion. The measurement [15] of the excitation function for ^{1}H$(^{17}$F,$p)^{17}$F revealed the elusive 3^+ state in ^{18}Ne, assumed for long time to play a role in explosive stellar cases [16]. Fusion cross sections for ^{17}F+^{208}Pb have been measured by Rehm *et al.* below the Coulomb barrier [17]. No enhancement has been found, mainly because Coulomb excitation and breakup probabilities at near-barrier energies are too small to influence the fusion process significantly. The interaction cross section has been measured by Ozawa, Suzuki, and Tanihata [18], and rms radii have been extracted for $A = 17$ isobars. No anomaly has been revealed for ^{17}F as discussed, e.g. in Ref. [19]. Finally, optical potentials for ^{17}F are of particular interest for interpreting measurements of the proton-transfer reaction ^{14}N$(^{17}$F,^{18}Ne$)^{13}$C, which aims to determine ANCs for ^{17}F+p and the ^{17}F$(p,\gamma)^{18}$Ne direct-capture cross section that is important in novae [20].

We present measurements of the ^{14}N$(^{17}$F,^{17}F$)^{14}$N and ^{12}C$(^{17}$F,^{17}F$)^{12}$C elastic-scattering cross sections in Sec. II. Analysis of the data and optical-model potentials is presented in Sec. III. Conclusions are summarized in Sec. IV.

II. THE EXPERIMENT

The measurements were performed at the Holifield Radioactive Ion Beam Facility (HRIBF) with an isotopically pure beam of ^{17}F. The ^{17}F was produced by the ^{16}O$(d,n)^{17}$F reaction in a thick hafnium-oxide target and ionized by a kinetic-injection negative ion source [8]. The ^{17}F beam was accelerated to an energy of 170 MeV by the HRIBF tandem accelerator and then poststripped to $q = 9^+$ to remove the ^{17}O isobaric contamination from the beam. The ^{17}F beam bombarded polypropylene $(CH_2)_n$ and melamine $(C_3N_6H_6)$ targets. A 2.2-mg/cm^2-thick polypropylene target was used to measure the ^{12}C$(^{17}$F,^{17}F$)^{12}$C elastic-scattering cross section. A somewhat thinner 1.0-mg/cm^2 target of melamine was used to measure the ^{14}N$(^{17}$F,^{17}F$)$ ^{14}N cross section, which allowed the elastic scattering from ^{12}C and ^{14}N in the target to be resolved by energy at some angles. The target thicknesses were determined by measurement of the energy loss of α particles through the target and by weighing in the case of the polypropylene target. The beam intensity on target varied between 6×10^5 s^{-1} and 2×10^6 s^{-1}.

In one set of measurements, charged particles were detected by two position-sensitive silicon-strip detector telescopes (25 cm^2 in area), symmetrically positioned around the beam axis, covering $\theta_{\rm lab} = 3^\circ - 9^\circ$. Thin (65-$\mu$m) ΔE detectors were backed by 300-μm-thick detectors. This detector configuration allowed identification of the Z of the scattered charged particles, though this was not significant for extraction of the elastic-scattering cross sections because of the strong dominance of the charged-particle yield by elastic scattering. The efficiency and position and energy spectra of the detectors were calibrated by measurement of elastic scattering from a gold foil with masks collimating the angles viewed by the detectors. The absolute normalization of the cross section at the most forward angles ($\theta_{\rm lab} < 5^\circ$) was determined by reduction of the incident-beam intensity to about 10^4 s^{-1} and detection of each incident-beam ion in a large-area silicon detector placed at $\theta_{\rm lab} = 0^\circ$ just downstream of the position-sensitive detectors. The cross section at $5^\circ < \theta < 9^\circ$ was determined by normalization to this forward-angle-scattering cross section.

A second set of measurements was also performed to extend the angular range of the elastic-scattering distributions. The Silicon-strip Detector Array (SIDAR) [21] was used in these measurements to cover laboratory angles $\theta_{\rm lab} = 7^\circ - 18^\circ$ in 16 angular bins. The angular coverage of SIDAR was determined by measurements with a calibrated α source and by the well-known geometry of the array. Absolute normalizations for the cross sections were determined for the most forward-angle strips in SIDAR ($\theta < 9^\circ$) by use of a technique similar to that just described. For laboratory angles of about 12° or less, elastic scattering from ^{12}C and from ^{14}N in the melamine target could not be distinguished. The yield of ^{12}C+^{17}F elastic scattering from the melamine target was determined at each angle with the measured ^{12}C$(^{17}$F,^{17}F$)^{12}$C cross section and the well-characterized detector response. The contribution from ^{12}C+^{17}F scattering was subtracted from the raw melamine spectra, and the net yields were extracted to determine the ^{14}N$(^{17}$F,^{17}F$)^{14}$N cross section. Good agreement was found between the calculated ^{17}F+^{12}C yields and the observed yields at larger laboratory angles at which scattering from ^{12}C and ^{14}N could be distinguished. Examples of the raw spectra from the melamine target at two laboratory angles are shown in Fig. 1, along with the calculated yields for the ^{12}C$(^{17}$F,^{17}F$)^{12}$C reaction that were subtracted to determine the net ^{14}N$(^{17}$F,^{17}F$)^{14}$N yields.

The data obtained on both targets are shown in Fig. 2 in the two upper curves. The good energy resolution and low emittance of the tandem beam allowed the differential cross section to be measured with good resolution, allowing for full identification of the typical Fraunhofer oscillations at small angles. The present data are comparable in quality with data obtained with stable beams and good magnetic spectrometers (lowest curve in Fig. 2, data from Ref. [22]), and they have better angular resolution and a larger angular range than previous elastic-scattering data obtained with RNBs (see, e.g. [1–3,23]).

III. OPTICAL POTENTIALS

Optical potentials were determined by use of a folding model with the nuclear matter approach of JLM [5]

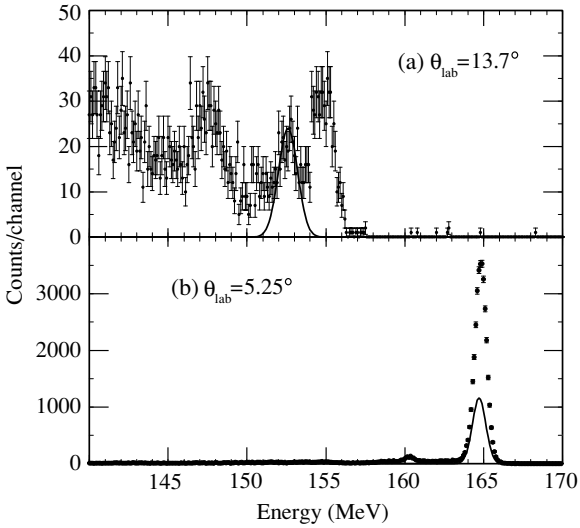

FIG. 1. Examples of the raw charged-particle spectra by use of a melamine target (a) at $\theta_{lab} = 13.7^\circ$ collected with the SIDAR array and (b) at $\theta_{lab} = 5.25^\circ$ collected with position-sensitive silicon-strip detectors. The highest energy peak corresponds to (a) ^{14}N(^{17}F,^{17}F)^{14}N and (b) a combination of ^{14}N(^{17}F,^{17}F)^{14}N and ^{12}C(^{17}F,^{17}F)^{12}C scattering. The solid curve in each case shows the expected contribution from ^{12}C(^{17}F,^{17}F)^{12}C elastic scattering.

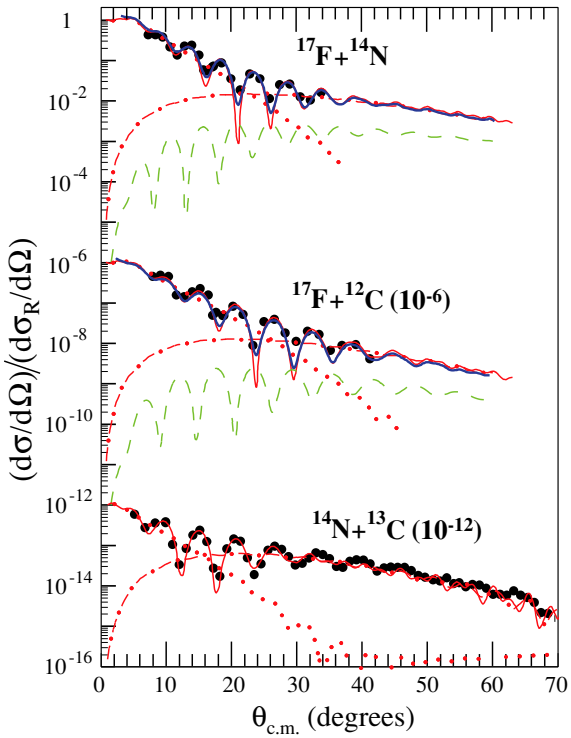

FIG. 2. (Color online) Elastic-scattering data (filled circles) for ^{17}F+^{14}N and ^{17}F+^{12}C at 10 MeV/nucleon. Previous data for ^{14}N+^{13}C at 12 MeV/nucleon are shown for comparison in the lowest graph [22]. The thin curves are calculated with the JLM parameters from Table II and then convoluted with detector angular resolution (thick curves). Far-side and near-side cross sections are indicated by dash-dotted and dotted curves, respectively. The calculated inelastic-scattering cross sections, ^{14}N(^{17}F,^{17}F*)^{14}N and ^{12}C(^{17}F,^{17}F*)^{12}C, to the first excited state in ^{17}F are indicated by dashed curves.

that incorporates a complex energy- and density-dependent parametrization of the effective interaction obtained in the Brueckner Hartree-Fock approximation from the Reid hard-core nucleon-nucleon (*NN*) potential. In the JLM model the complex form factor for the optical potential is given by

$$U(R) = \int d\vec{r}_1 d\vec{r}_2 \rho_1(r_1)\rho_2(r_2)v(\rho, E, s), \qquad (1)$$

where $v(\rho, E, s)$ is the (complex) effective *NN* interaction, $\vec{R}$ is the separation between nuclei, $\rho_{1(2)}$ are the single-particle densities of the interacting partners, $\vec{s} = \vec{r}_1 + \vec{R} - \vec{r}_2$ is the *NN* separation distance between the interacting nucleons, and ρ is the overlap density. Because the local-density approximation used in Eq. (1) does not represent properly the surface effects in finite nuclei, and to increase the flexibility of the folding potential, a smearing function has been introduced [5], such that

$$\tilde{U}(R) = \int d\vec{R}' U(R') g(|\vec{R} - \vec{R}'|) \qquad (2)$$

is our final folding potential. The smearing function $g(r)$ is taken as a normalized Gaussian [5,6],

$$g(r) = \frac{1}{t^3 \pi^{3/2}} \exp(-r^2/t^2), \qquad (3)$$

which tends to a δ function for $t \to 0$, whereas for finite t values it increases the rms radius of the folding form factor by $r_g^2 = (3/2)t^2$, leaving unchanged the volume integral. It turns out that the smearing procedure already described is essential in simulating the complicated radial dependence of the dynamic polarization potential. To be consistent with the JLM model we take the overlap density in Eq. (1) as

$$\rho = \left[\rho_1\left(\vec{r}_1 + \frac{1}{2}\vec{s}\right)\rho_2\left(\vec{r}_2 - \frac{1}{2}\vec{s}\right)\right]^{1/2}. \qquad (4)$$

This approximation is physically appealing because the overlap density tends to zero when one of the interacting nucleons is far from the bulk, and to the nuclear matter saturation value at complete overlap. It should be noted that originally the JLM model was developed to describe nucleon-nucleus optical potentials, and its density dependence is calibrated for densities not exceeding the saturation value in nuclear matter [5].

In the earlier analysis [6], we used fixed values for the range parameters $t_V = 1.20$ fm and $t_W = 1.75$ fm, found from a global analysis of the data. Only the renormalization factors N_V and N_W were left free in the fits for each case. In the present analysis with double-folded potentials, all four parameters have been searched simultaneously to fit the data for each case: two strength parameters (N_V and N_W) and two range parameters (t_V and t_W),

$$U_{DF}(r) = N_V V(r, t_V) + i N_W W(r, t_W), \qquad (5)$$

to obtain a phenomenological representation of the DPP as a uniform renormalization of the depths and radii of the folding potentials.

Previously we used densities obtained from HF+BCS calculations, carefully tuned to give the correct total binding energy of each partner. However, it is known that mean-field approximations are not accurate enough to reproduce the empirical single-particle energies for weakly bound nuclei. Therefore realistic densities for such nuclei could be obtained only with hybrid methods. Here we used for ^{17}F and ^{14}N densities calculated as $\rho = \rho_{\rm core} + \rho_{\rm sp}$, where $\rho_{\rm core}$ is the HF+BCS density for the well-bound core nucleus and $\rho_{\rm sp}$ is the single-particle density calculated from the wave function of the last proton that has the asymptotic behavior given by the ANCs extracted from experiment. For the ground state in ^{17}F we used $C^2_{1d_{5/2}} = 1.08(10)$ fm^{-1}, as obtained from the reaction ^{16}O(^{3}He,d)^{17}F [11]. With this value the corresponding single-particle rms radius is 4.45±0.42 fm [24], about two times larger than the core radius. For ^{14}N we used $C^2_{1p_{1/2}} = 18.6(12)$ fm^{-1} and $C^2_{1p_{3/2}} = 0.93(14)$ fm^{-1} for the two main components in its ground state, as obtained from the reaction ^{13}C(^{14}N,^{13}C)^{14}N [22]. The core (^{16}O, ^{13}C) and the target (^{12}C) densities have been estimated in a standard spherical HF+BCS approximation by use of the density functional of Beiner and Lombard [25]. The rms radii for the proton (r_p), neutron (r_n), and matter (r_m) distributions are summarized in Table I and compared with values for matter and charge ($r_{\rm ch}$) radii extracted from high-energy reaction data [18] and electron scattering [26]. Although HF and HF+ANC methods predict almost identical proton rms radii, the corresponding densities behave rather differently at large distances, as can be seen in Fig. 3. It would be interesting if one can isolate the effect of the enhanced density tail of ^{17}F in elastic-scattering distributions. This would be possible only if the absorption near the barrier is small.

TABLE I. Root-mean-square radii of the single-particle densities from HF and HF+ANC methods, as described in the main text. Results from a HF calculation with Skyrme SGII parametrization of the interaction are also given for comparison in the last line. Experimental radii from high-energy reaction data and from electron scattering are also included for comparison. Dimensions of all radii are in fm.

Nucleus	r_p	r_n	r_m	r_m(exp)[a]	$r_{\rm ch}$(exp)[b]
^{17}F (HF+BCS)	2.79	2.65	2.73	2.54±0.08	
^{16}O (HF+BCS)	2.65	2.63	2.64	2.54±0.02	2.70±0.008
^{14}N (HF+BCS)	2.60	2.58	2.59	2.47±0.03	2.55±0.008
^{13}C (HF+BCS)	2.48	2.58	2.53	2.28±0.04	2.46±0.003
^{12}C (HF+BCS)	2.44	2.43	2.43	2.35±0.02	2.47±0.002
^{17}F (HF+ANC)	2.81	2.63	2.73		
^{14}N (HF+ANC)	2.52	2.58	2.55		
^{17}F (HF+SGII)[c]	2.72	2.61	2.67		

[a]Reference [18].
[b]Reference [26].
[c]Reference [19].

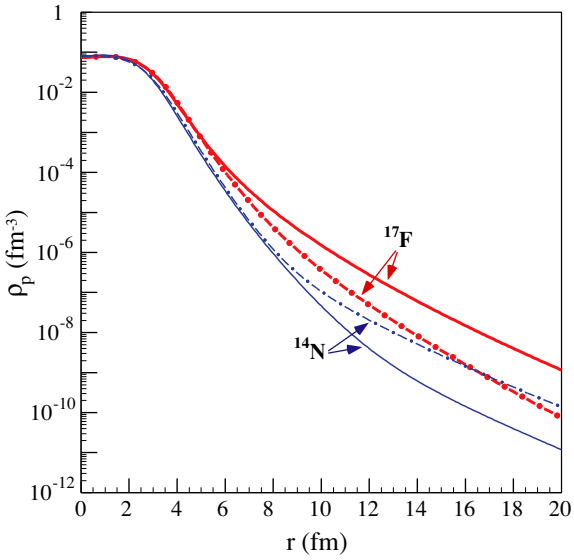

FIG. 3. (Color online) Proton densities for ^{17}F and ^{14}N calculated with HF (dash-dotted curves) and ANC method (solid curves).

The elastic-scattering angular distributions show rapid oscillations at small angles which decrease in amplitude with the increasing scattering angle. Assuming pure Fraunhofer scattering at forward angles, we extract grazing angular momenta of $l_g \approx 35$ and 30 from the angular spacing $\Delta\theta = \pi/(l_g + 1/2)$ for ^{14}N and ^{12}C targets respectively. The classical closest approach at grazing is on average $R_g \approx 7.2$ fm, whereas the estimated strong absorption radius is slightly larger, $R_s \approx 7.3$ fm. Apparently we are faced with almost classical distant collisions in the presence of significant absorption. Similarities seen in the differential cross sections in Fig. 2 indicate general wave-mechanical characteristics of the scattering process and average systematic properties of the nuclear interaction.

The JLM calculation with both HF and HF+ANC densities give nearly identical cross sections. Only the latter are shown in Fig. 2, with parameters given in Table II. The calculated cross section was convoluted with a Gaussian detector response function with a width (full-width half-maximum) of $\Delta\theta_{\rm c.m.} = 1.2^\circ$ to approximate the finite angular bins of the experimental data. The smoothed cross section is also shown in Fig. 2. The errors in Table II represent the deviation needed to increase the best-fit χ^2 by one unit. Varying the range parameters from the "standard" values did not result in improved fits to the data, so we adopt $t_V = 1.20$ fm, and $t_W = 1.75$ fm, found from the previous global analysis. The cross section at the most forward angles is not sensitive to the choice of the optical potential. The theoretical cross section agrees with the data at the most forward angles within a few percent, verifying the overall normalization of the cross sections. The contribution of inelastic scattering of ^{17}F ($J^\pi = 1/2^+$, $E_x = 495$ keV) was calculated with the deformation length extracted from the electromagnetic transition probability $B(E2)\uparrow = 21.64\, e^2$ fm^4 [27] and is in Fig. 2. The inelastic-scattering cross section was found to be at least 1-order of magnitude smaller than the elastic cross section at all angles and was ignored in subsequent analysis.

TABLE II. Best-fit parameters (t_V, t_W, N_V, N_W) from the double-folding analysis described in the text. The Coulomb component is calculated by folding charge distributions (Table I). The real and imaginary volume integrals (J_V and J_W, respectively), the real and imaginary rms radii (R_V and R_W, respectively), the total reaction cross section (σ_R), and χ^2's for the fits are also tabulated.

Reaction	Energy (MeV)	t_V (fm)	t_W (fm)	N_V	N_W	χ^2	σ_R (b)	J_V (MeV fm^3)	J_W (MeV fm^3)	R_V (fm)	R_W (fm)
^{17}F+^{14}N	170	1.20	1.75	0.63±0.06	0.90±0.07	9.9	1.77	351	107	4.31	4.82
^{17}F+^{12}C	170	1.20	1.75	0.51±0.05	0.98±0.08	5.1	1.69	288	118	4.22	4.73
^{14}N+^{13}C[a]	162	1.20	1.75	0.42±0.01	0.83±0.02	8.8	1.56	234	107	4.16	4.61

[a]Data from Ref. [6].

The parameters listed in Table II indicate a slightly larger normalization of the real potential as compared with the global set for *p*-shell nuclei found in [6], but again the normalization of the absorptive part approaches unity. The dynamic polarization potential is less repulsive than expected because the proton removal channel is suppressed by the centrifugal barrier ($l = 2$). This would indicate a slightly increased refraction that is due to enhanced density tails of both projectile and target. However, the usual notch test with a Gaussian spike placed at selected mesh points showed that the cross section is sensitive to only a narrow radial range, $r = 6$ to 7 fm, close to the strong absorption radius. Only the diffuse edge of the potential in the barrier region contributes to the scattering. The dominance of the far-side component beyond the Fraunhofer crossing angle (Fig. 2) indicates a normal diffractive shadow that is due purely to absorption. The leveling off of the cross section at large angles arises from the Sommerfeld edge waves generated at the periphery of the nucleus by the passing beam.

The effect of incomplete absorption is shown in Fig. 4. The strength of the imaginary part of the optical potential is reduced artificially by factors shown in the figure until the real potential becomes strong enough to produce a nuclear rainbow. Only at one quarter of the nominal absorption do characteristic broad Airy oscillations appear on the bright side of the nuclear rainbow. These structures are carried entirely by the far-side component, as a manifestation of the refractive power of the real potential. Unfortunately, the nominal absorption completely damps these structures and only modest traces survive at large angles.

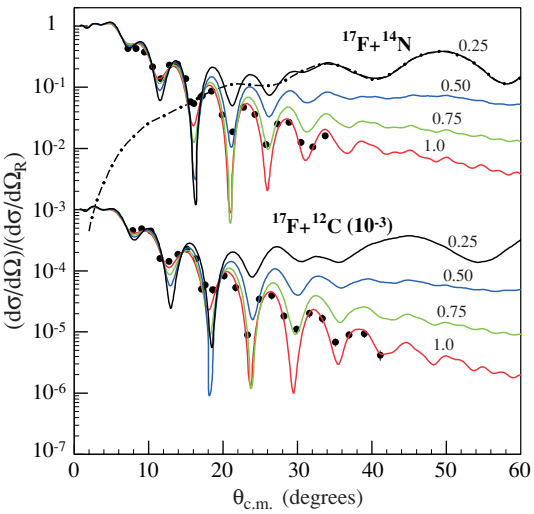

FIG. 4. (Color online) The measured ^{17}F+^{14}N and ^{17}F+^{12}C elastic-scattering cross sections are compared with calculations with varying strengths of the imaginary potential to show the effect of incomplete absorption. The lowest curves for each reaction (label 1.0) were calculated by use of the JLM potential with parameters from Table II and are the same as those shown in Fig. 2. The other solid curves were calculated with reduced renormalization factors for the imaginary potential of $N_W = 0.75, 0.50, 0.25$. The dash-dotted curve is the far-side cross section for $N_W = 0.25$ for ^{17}F+^{14}N scattering.

We also performed an analysis in terms of conventional Woods-Saxon form factors for the nuclear term,

$$U(r) = -[V_0 f_V(r) + i W_0 f_W(r)], \tag{6}$$

where

$$f_V(r) = \left\{1 + \exp\left[\frac{r - r_V\left(A_1{}^{1/3} + A_2{}^{1/3}\right)}{a_V}\right]\right\}^{-1}, \tag{7}$$

with r_V being the reduced radius of the real potential and a_V the diffuseness. The imaginary part of the potential, $f_W(r)$, is similarly defined in terms of the parameters for the reduced radius and diffuseness, r_W and a_W, respectively. The nuclear potential was supplemented with a Coulomb term generated by a uniform charge distribution with a reduced radius fixed to $r_c = 1$ fm. No preference has been found for volume or surface-localized absorption, and we kept only volume absorption. Gridding on the real potential depth (V_0) and searching on all other parameters resulted in considerable continuous ambiguity. We obtained solutions of similar quality with practically any potential with a real volume integral in the range 150–400 MeV fm^3. The imaginary potential is more stable, resulting in an almost unique reaction cross section for each reaction studied here. Optical-model potentials with real volume integrals similar to that predicted by the folding model are listed in Table III. In addition to the best-fit parameters for the depth (V_0, W_0), reduced radius (r_V, r_W), and diffuseness (a_V, a_W), the volume integral per pair of interacting nucleons (J_V, J_W), and rms radii (R_V, R_W) are tabulated for both (real, imaginary) parts of the potential. The total reaction cross section, σ_R, and total χ^2 for the fit are also given in Table III. We obtain systematically $r_V < r_W$ and large diffuseness parameters (~0.7) in agreement with theoretical expectations for loosely bound nuclei [28]. Using the strong absorption model of Kox *et al.* [29] and the reaction cross sections given in Table III, we extract a reduced strong absorption radius $r_0 = 1.175$ fm, larger than the standard value for stable nuclei ($r_0 = 1.10$ fm). Note that the "meager" variation of $\delta r_0 = 0.075$ leads to an increase of the reaction cross section by ~200 mb.

TABLE III. Woods-Saxon parameters [V_0, W_0, r_V, r_W, a_V, and a_W as defined in Eqs. (6) and (7)] determined from a best fit to the elastic-scattering data. The Coulomb reduced radius was fixed to $r_c = 1$ fm. The volume integrals, rms radii, total reaction cross sections, and χ^2's for the fits are also tabulated.

Reaction	Energy (MeV)		V_0 (MeV)	W_0 (MeV)	r_V (fm)	r_W (fm)	a_V (fm)	a_W (fm)	χ^2	σ_R (b)	J_V (MeV fm^3)	J_W (MeV fm^3)	R_V (fm)	R_W (fm)
^{17}F+^{14}N	170	(A)	151.40	24.93	0.968	1.15	0.696	0.697	10.0	1.73	350	94	4.54	5.14
		(B)	198.88	25.75	0.930	1.15	0.696	0.679	10.3	1.72	425	97	4.42	5.11
^{17}F+^{12}C	170	(A)	146.66	23.66	0.909	1.15	0.717	0.720	6.2	1.68	327	99	4.34	5.09
		(B)	190.57	23.74	0.887	1.15	0.692	0.719	5.7	1.68	393	99	4.21	5.09

The far-side dominance at large angles seen in Fig. 2 is the rule rather than the exception in heavy-ion scattering. The observation of a Fraunhofer crossover where F/N interference oscillations reach their maximum amplitude sometimes determines the strength of the real potential [30]. The simple decomposition of the scattering amplitude into traveling waves does not give any information about the incident flux penetrating the barrier. The semiclassical uniform approximation for the scattering amplitude of Brink and Takigawa [31] is well adapted to describe situations in which the scattering is controlled by at most three active, isolated, complex turning points. An approximate multireflection series expansion of the scattering function can be obtained, the terms of which have the same simple physical meaning as in the exact Debye expansion for the scattering of light by a spherical well. The major interest in this theory comes from the fact that it can give precious information on the response of a nuclear system to the nuclear interior.

In this technique, the semiclassical scattering function is decomposed as

$$S_{\mathrm{WKB}}(l) = S_B(l) + S_I(l), \tag{8}$$

where $S_B(l)$ is the barrier term that describes the flux reflected at the barrier and $S_I(l)$ is the internal barrier component that describes the flux penetrating the barrier and reflected and refracted several times between internal turning points.

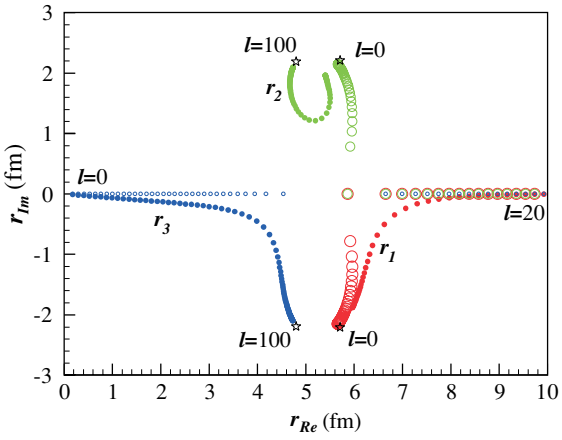

FIG. 5. (Color online) Complex turning points (filled symbols) for the potential "A" in Table III. Open symbols denote complex turning points for the real potential alone. Stars indicate complex poles of the potential.

The corresponding total scattering amplitude is decomposed likewise as $f_{\mathrm{WKB}} = f_B + f_I$ and the angular distributions as $\sigma_{B(I)} = |f_{B(I)}|^2$ by use of the usual angular momentum expansion of the amplitudes. The $B(I)$ components are calculated from classical action integrals along complex paths between turning points; see [4,31] for details. We take as an example ^{17}F+^{14}N and the potential "A" in Table III. Trajectories of complex turning points are shown in Fig. 5. Only turning points close to the real axis have been retained. We found a typical situation with three isolated turning points, as the effective potential (real+centrifugal) is sufficiently strong to sustain a pocket up to grazing angular momentum. We use standard notation, e.g., r_1 denotes the outermost turning point and r_3 the innermost one. The absorption plays an important role in these complex trajectories. When the imaginary part of the potential is removed, the points $r_{1,2}$ become complex conjugates and coalesce on the real axis for angular momenta in excess of the grazing value.

Absorption profiles are shown in Fig. 6. First one observes that the semiclassical B/I expansion (solid curve) is an *exact*

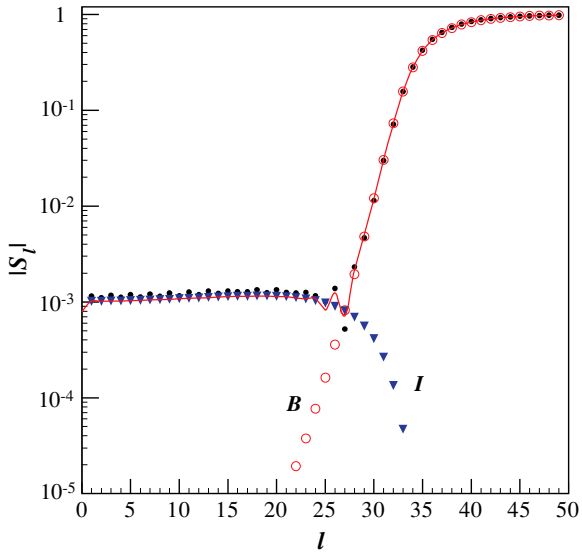

FIG. 6. (Color online) Semiclassical decomposition of the scattering function for the Woods-Saxon potential "A" in Table III. Barrier (open circles) and internal barrier components (triangles) are indicated. The exact total quantum S-matrix elements are indicated by small black dots. The solid curve is a cubic spline interpolation of the total semiclassical scattering function for the same potential.

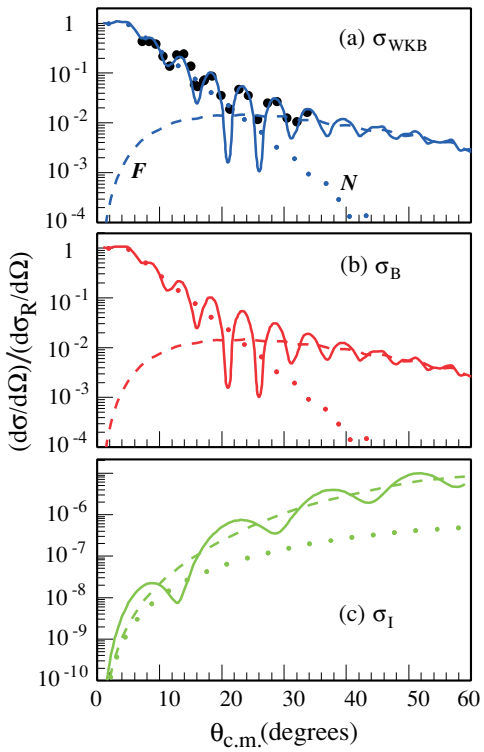

FIG. 7. (Color online) The measured ^{17}F+^{14}N elastic-scattering cross section is compared with (a) the semiclassical WKB cross section [31] by use of potential "A" from Table III. The WKB cross section is decomposed into (b) semiclassical barrier (σ_B) and (c) internal barrier (σ_I) components. The barrier component σ_B is virtually identical to the full WKB cross section. The far-side (dashed curve) and near-side (dotted curve) contributions are also shown in each case.

decomposition of the quantum result (black dots). The barrier profile (open circles) resembles the strong absorption profile, and this justifies the interpretation that it corresponds to that part of the incident flux not penetrating the nuclear interior. The internal component (triangles) has nonvanishing values up to grazing angular momentum and is completely negligible beyond this value. The average value for $l \leqslant l_g$ is $|S_I| \approx 10^{-3}$, 2 orders of magnitude fewer than for ^{6}Li+^{12}C at 9 MeV/nucleon [4].

Semiclassical cross sections are compared with the data in Fig. 7 for the reaction ^{17}F+^{14}N. Similar results have been obtained for the other reaction. All components have been further decomposed into far-side/near-side (F/N) subcomponents by use of standard techniques. In the middle panel, the barrier cross section is virtually identical to the full WKB cross section. The reason is that the internal barrier component is negligibly small for the range of angles measured in this paper. Therefore almost no traces of refractive effects survive in the cross section. The scattering is completely absorptive. The Fraunhofer pattern in the data is carried entirely by the barrier component, with strong oscillations generated by F/N interference.

IV. CONCLUSIONS

We measured precision data for elastic scattering of ^{17}F on two light targets at 10 MeV/nucleon. The double-folding potentials, by use of density- and energy-dependent *NN* effective interactions and realistic densities that incorporate structure information through the measured asymptotic normalization coefficients, provide an excellent description of the data. The slightly enhanced density in the tails leads to a modest enhancement of the normalization of the real optical potential. Both folding and barrier–internal barrier techniques point to the conclusion that the scattering is completely absorptive. The scattering process is determined mainly by the reflection on the diffuse tail of the potential, and this explains the considerable ambiguity in finding reasonable Woods-Saxon potentials. This points clearly to a peripheral character of the scattering, a very favorable situation for the using the proton transfer reactions and the ANC method for nuclear astrophysics.

The JLM double-folding model is in principle a four-parameter model. However, we found that the imaginary part does not need any renormalization ($N_W \approx 1.0$), which seems a rather general situation for *p*-shell nuclei [1–3,6]. Moreover, the standard range parameters $t_v = 1.20$ fm and $t_w = 1.75$ fm [6] give the best description of the present data. Therefore we are left with a single ajustable parameter (N_V) in a limited range of values, 0.4–0.6. This is very encouraging for situations in which good optical potentials could not be extracted from limited elastic angular distributions.

ACKNOWLEDGMENTS

ORNL is managed by UT-Battelle, LLC, for the U.S. Department of Energy under contract DE-AC05-00OR22725. This work was supported in part by the U.S. Department of Energy under grants DE-FG03-93ER40773, DE-FG02-96ER40955, DE-FG02-93ER40789, and DE-FG02-88ER40387; by the Romanian Ministry for Education, Research and Youth under contract no. 555/2000, and by the Robert A. Welch Foundation. The authors thank the staff of the HRIBF whose hard work and support made these measurements possible. One of the authors (F.C.) acknowledges the support of the Cyclotron Institute, Texas A&M University, for part of the time this work was done.

[1] A. Azhari, V. Burjan, F. Carstoiu, C. A. Gagliardi, V. Kroha, A. M. Mukhamedzhanov, F. M. Nunes, X. Tang, L. Trache, and R. E. Tribble, Phys. Rev. C **63**, 055803 (2001).
[2] X. Tang, A. Azhari, C. A. Gagliardi, A. M. Mukhamedzhanov, F. Pirlepesov, L. Trache, R. E. Tribble, V. Burjan, V. Kroha, and F. Carstoiu, Phys. Rev. C **67**, 015804 (2003).
[3] X. Tang *et al.*, Phys. Rev. C **69**, 055807 (2004).
[4] F. Carstoiu, L. Trache, R. E. Tribble, and C. A. Gagliardi, Phys. Rev. C **70**, 054610 (2004).

[5] J. P. Jeukenne, A. Lejeune, and C. Mahaux, Phys. Rev. C **16**, 80 (1977).
[6] L. Trache, A. Azhari, H. L. Clark, C. A. Gagliardi, Y.-W. Lui, A. M. Mukhamedzhanov, R. E. Tribble, and F. Carstoiu, Phys. Rev. C **61**, 024612 (2000).
[7] B. Harss *et al*., Phys. Rev. C **65**, 035803 (2002).
[8] R. F. Welton *et al*., Nucl. Instrum. Methods Phys. Res. B **159**, 116 (1999).
[9] C. Iliadis *et al*., Astrophys. J. Suppl. Ser. **142**, 105 (2002).
[10] R. Morlock, R. Kunz, A. Mayer, M. Jaeger, A. Müller, J. W. Hammer, P. Mohr, H. Oberhummer, G. Staudt, and V. Kölle, Phys. Rev. Lett. **79**, 3837 (1997).
[11] C. A. Gagliardi *et al*., Phys. Rev. C **59**, 1149 (1999).
[12] J. F. Liang *et al*., Phys. Rev. C **65**, 051603(R) (2002).
[13] J. F. Liang *et al*., Phys. Rev. C **67**, 044603 (2003).
[14] M. Romoli *et al*., Phys. Rev. C **69**, 064614 (2004).
[15] D. W. Bardayan *et al*., Phys. Rev. Lett. **83**, 45 (1999).
[16] M. Wiescher, J. Görres, and K.-F. Thielemann, Astrophys. J. **326**, 384 (1988).
[17] K. E. Rehm *et al*., Phys. Rev. Lett. **81**, 3341 (1998).
[18] A. Ozawa, T. Suzuki, and I. Tanihata, Nucl. Phys. **A693**, 32 (2001), and references therein.
[19] H. Kitagawa, N. Tajima, and H. Sagawa, Z. Phys. A **358**, 381 (1997).
[20] J. C. Blackmon *et al*., Nucl. Phys. **A718**, 587 (2003).
[21] D. W. Bardayan *et al*., Phys. Rev. C **62**, 055804 (2000).
[22] L. Trache, A. Azhari, H. L. Clark, C. A. Gagliardi, Y.-W. Lui, A. M. Mukhamedzhanov, R. E. Tribble, and F. Carstoiu, Phys. Rev. C **58**, 2715 (1998).
[23] D. Peterson, J. J. Kolata, P. Santi, J. von Schwarzenberg, D. Bazin, and B. M. Sherrill, Phys. Rev. C **67**, 014601 (2003).
[24] L. Trache, A. Azhari, F. Carstoiu, C. A. Gaglicardi, A. M. Mukhamedzhanov, X. D. Tang, R. E. Tribble, and S. Zhou, Texas A & M University Cyclotron Institute Progress Report 2001–2002 (Texas A & M University, College Station, TX, 2002), p. 1–16.
[25] M. Beiner and J. R. Lombard, Ann. Phys. (NY) **86**, 262 (1974).
[26] I. Angeli, Acta Phys. Hungarica - Heavy Ion Phys. **8**, 23 (1998).
[27] D. R. Tilley *et al*., Nucl. Phys. **A564**, 1 (1993).
[28] M. S. Hussein and G. R. Satchler, Nucl. Phys. **A567**, 165 (1994).
[29] S. Kox *et al*., Phys. Rev. C **35**, 1678 (1987).
[30] K. W. McVoy and G. R. Satchler, Nucl. Phys. **A417**, 157 (1984).
[31] D. M. Brink and N. Takigawa, Nucl. Phys. **A279**, 159 (1977).